

Carbon monoxide in the solar atmosphere

I. Numerical method and two-dimensional models[★]

S. Wedemeyer-Böhm¹, I. Kamp², J. Bruls¹, and B. Freytag³

¹ Kiepenheuer-Institut für Sonnenphysik, Schöneckstraße 6, 79104 Freiburg, Germany
e-mail: wedemeyer@kis.uni-freiburg.de

² Space Telescope Division of ESA, STScI, 3700 San Martin Drive, Baltimore MD 21218, USA

³ Department for Astronomy and Space Physics, Uppsala University, Box 515, 75120 Uppsala, Sweden

Received 15 December 2004 / Accepted 21 March 2005

Abstract. The radiation hydrodynamic code CO5BOLD has been supplemented with the time-dependent treatment of chemical reaction networks. Advection of particle densities due to the hydrodynamic flow field is also included. The radiative transfer is treated frequency-independently, i.e. grey, so far. The upgraded code has been applied to two-dimensional simulations of carbon monoxide (CO) in the non-magnetic solar photosphere and low chromosphere. For this purpose a reaction network has been constructed, taking into account the reactions that are most important for the formation and dissociation of CO under the physical conditions of the solar atmosphere. The network has been strongly reduced to 27 reactions, involving the chemical species H, H₂, C, O, CO, CH, OH and a representative metal. The resulting CO number density is highest in the cool regions of the reversed granulation pattern at mid-photospheric heights and decreases strongly above. There, the CO abundance stays close to a value of 8.3 on the usual logarithmic abundance scale with [H] = 12 but is reduced in hot shock waves which are a ubiquitous phenomenon of the model atmosphere. For comparison, the corresponding equilibrium densities have been calculated, based on the reaction network but also under the assumption of instantaneous chemical equilibrium by applying the Rybicki & Hummer (RH) code. Owing to the short chemical timescales, the assumption holds for a large fraction of the atmosphere, in particular the photosphere. In contrast, the CO number density deviates strongly from the corresponding equilibrium value in the vicinity of chromospheric shock waves. Simulations with altered reaction networks clearly show that the formation channel via hydroxide (OH) is the most important one under the conditions of the solar atmosphere.

Key words. Sun: chromosphere – Sun: photosphere – hydrodynamics – radiative transfer – astrochemistry

1. Introduction

Since Noyes & Hall (1972b) deduced very low brightness temperatures in the (upper) photosphere from observations in the core of the carbon monoxide (CO) 3–2 R14 line, the thermal structure of this layer has been subject of an ongoing controversial debate. In many subsequent observations the low temperatures have not only been confirmed, e.g. by Ayres & Testerman (1981), but also found to be as low as 4000 K and even down to only 3700 K (see Figs. 4–5 in Ayres & Testerman 1981). These small values fall below the values implied by commonly used semi-empirical models like VAL-C (Vernazza et al. 1981) that are based on other diagnostics, e.g., in the UV range. Moreover, the CO observations did not show a prominent temperature inversion which is an important feature of VAL-C-like models. Ayres & Testerman explained this “diagnostic dilemma” with the thermal bifurcation of the outer solar layers. Following that idea, the hot plasma would be confined in discrete structures

embedded in cool gas that can account for the observed carbon monoxide features. The inhomogeneities would be preferably of small spatial scale and large thermal contrast.

A number of investigations imply that the bulk of CO is located in the low chromosphere and below. For instance, Ayres & Testerman state that the CO concentration peaks at an optical depth of $\tau_{500} \lesssim 10^{-2}$ for a reference wavelength of 500 nm. That is in line with the results by Solanki et al. (1994) who observed CO in emission at the solar limb. There, it remains at a constant level up to 0''4 (≈ 300 km) above the (continuum) limb before it decreases rapidly in the layers above (see their Fig. 2). Uitenbroek et al. (1994) carried out similar observations, but with an improved technique, and found CO in emission, extending 0''5 (≈ 360 km) beyond the continuum limb. Ayres & Rabin (1996) derive, based on the $\Delta V = 1$ bands, an off-limb extension of 0''6 (≈ 440 km) for the strongest lines, indicating the presence of cool gas up to 350 km above the classical temperature minimum.

Given the high temperatures implied by other diagnostics, the above-mentioned CO observations inevitably demand

[★] Movie material and PS file are only available in electronic form at <http://www.edpsciences.org>

a spatially inhomogeneous structure of the photosphere and low chromosphere. In this sense, Solanki et al. (1994), based on observed horizontal velocities, suggest that the bulk of CO might be located above granule interiors. Direct evidence for this assumption was provided by Uitenbroek (2000, see also Uitenbroek et al. 1994), who took spectroheliograms in the cores of CO lines. They discovered not only a pattern connected to the magnetic network, but also bright rings with dark centres in the quiet Sun, resembling a reversed granular pattern. Moreover, they conclude that such spatial variations are largely of dynamic nature, and that dynamics thus play an important role in the formation of the dark CO line cores. In fact, oscillatory intensity changes (see, e.g., Ayres 2004) have already been detected by Noyes & Hall (1972b).

A number of static models have been constructed in order to explain the observations, ranging from pure 1D atmospheres like the COmosphere (Wiedemann et al. 1994) to two-component models (e.g. Ayres et al. 1986; Ayres & Rabin 1996) and even more complex spatial configurations (e.g. Ayres 1991, 2002). But although indicating the right direction, the obvious dynamic nature of CO features cannot be reproduced by means of a static approach. Spatial *and* temporal variations have to be taken into account for a detailed model.

Instead of inverting observed intensities to a temperature stratification with one or more components, Uitenbroek (2000) started from a snapshot of the 3D hydrodynamical model by Stein & Nordlund (1989) and calculated CO number densities under the assumption of instantaneous chemical equilibrium (ICE). The highest concentration was found in the middle photosphere (~100–300 km above optical depth unity) above granule interiors, while the concentrations above intergranular lanes (at the same height) are 3–4 times smaller. The CO distribution is strongly connected to the cooling due to strong adiabatic expansion and cooling above the granule centres. The calculations were performed under the assumption of instantaneous chemical equilibrium. Neither the radiative cooling action by CO itself nor advection due to the hydrodynamic flow were taken into account. This pioneering work showed the importance of solar granulation for CO line formation.

Asensio Ramos et al. (2003) proceed to non-equilibrium CO chemistry calculations based on the time-dependent hydrodynamic simulations by Carlsson & Stein (1997). Solving the chemistry equations for a chemical reaction network, including the most relevant species, resulted in CO number density as a function of height and time. From this Asensio Ramos et al. conclude that the radiation in CO lines close to the solar limb originates from heights not greater than 700 km. Moreover, they proved that ICE is a valid assumption for the lower layers but overestimates the CO number densities above the low chromosphere. The calculations were one-dimensional only and thus did not allow for an analysis of the horizontal distribution.

This paper is the first in a series. Here we present time-dependent CO chemistry as part of multi-dimensional radiation hydrodynamics simulations, starting with the 2D case. The major advance with respect to earlier investigations is the time-dependent treatment of a chemical network in combination with advection of particle densities with the hydrodynamic flow in two or three spatial dimensions. The upgraded

code CO⁵BOLD (Freitag et al. 2002) will serve as a basis for further improvements, e.g., the back reaction of CO as a cooling agent.

After the description of the methods, the chemical input data and the numerical model in Sects. 2–4, respectively, we present the results of two-dimensional simulations in Sect. 5 which are discussed in Sect. 6. Our conclusions are drawn in Sect. 7.

2. Numerical method

2.1. Formulation of the problem

The number density n_i of a chemical species within a fixed volume can change in time (t) due to advection as expressed by the continuity equation:

$$\frac{\partial n_i}{\partial t} + \nabla \cdot (n_i \mathbf{v}) = 0, \quad (1)$$

where \mathbf{v} denotes the velocity of the hydrodynamic flow. An additional source term must be taken into account if the number density also changes due to chemical reactions. Such changes can be realised by a large variety of reactions. In the present application we restrict ourselves to two- and three-body reactions. The new term can then be written as

$$\begin{aligned} \left(\frac{\partial n_i}{\partial t} \right)_{\text{chem}} = & -n_i \sum_j k_{2,ij} n_j \\ & + \sum_j \sum_l k_{2,jl} n_j n_l \\ & -n_i \sum_j \sum_l k_{3,ijl} n_j n_l \\ & + \sum_j \sum_l \sum_m k_{3,jlm} n_j n_l n_m \end{aligned} \quad (2)$$

where n_i are the number densities of the different species. The first and second right-hand terms present two-body reactions which yield losses (negative sign) and gains (positive sign) for species density n_i with rates $k_{2,ij}$ and $k_{2,jl}$, respectively. Three-body reactions are analogously accounted for by the third and fourth term with rates $k_{3,ijl}$ and $k_{3,jlm}$. The resulting ordinary differential Eq. (2) is of first order and has to be imposed for each chemical species separately. The whole problem thus requires the solution of a system of differential equations.

Chemical reactions can have rates that differ by many orders of magnitude. Hence, not only the number densities of different species but also their temporal derivatives cover a large range, causing the system of equations to be stiff. Consequently, an implicit scheme should be used for the numerical solution of the problem.

2.2. Time-dependent solution

The time-dependent treatment of a chemical reaction network has been added as an optional separate computational step to the radiation hydrodynamics code CO⁵BOLD. The general properties of the code are described in Freitag et al. (2002) and Wedemeyer et al. (2004, hereafter W04). Following the general concept of operator splitting, the chemistry calculations

are performed after the hydrodynamics step for each computational time step. The treatment of advection and chemical reactions is thus separated into subsequent steps. First, the number densities of all chemical species are advected with the hydrodynamic flow field. This is done analogously to the gas density within the applied Roe solver. After the subsequent viscosity step the chemical reactions are handled for each grid cell separately, starting with the calculation of the reaction rates. Necessary input data are the local temperature, which is available as result of the hydrodynamics step, and the number densities of the involved chemical species of the previous time step. The basic rate is given by

$$k = \alpha T_{300}^{\beta} e^{-\gamma/T}, \quad (3)$$

where $T_{300} = T/300$ K. For catalytic reactions which involve a representative metal also the number density n_M of the metal enters:

$$k = n_M \alpha T_{300}^{\beta} e^{-\gamma/T}. \quad (4)$$

Given the rates, the system of differential equations is defined and then solved with an implicit BDF (backward differentiation formula) method. Here, the DVODE package is used (Brown et al. 1989). The solver uses an internal computational time step which is adjusted automatically. The solution provides the number densities of the involved species after the overall computational time step prescribed by the foregoing hydrodynamics.

The radiative transfer is treated in a subsequent step frequency-independently (grey) and under strict assumption of local thermodynamic equilibrium (LTE). See W04 for more details.

The boundary conditions are consistent with the hydrodynamics part of the code, i.e. in the presented simulations chemical species are advected across the lateral periodic boundaries and can leave the computational domain at top or bottom. As for the other boundary conditions, the number densities in the bottom grid layer are copied into the ghost cells below but are scaled to the mass density ρ of those cells:

$$\frac{\partial(n_i/\rho)}{\partial z} = 0 \quad \Leftrightarrow \quad n_i^{\text{ghost}} = n_i^{\text{bottom}} \rho^{\text{ghost}} / \rho^{\text{bottom}}. \quad (5)$$

This way the total particle numbers of the involved elements (here H, C, O and a representative metal M) are almost perfectly conserved, except for a decrease of typically 5×10^{-4} per simulation hour in relative number due to mass loss at the upper boundary.

2.3. Chemical equilibrium

In addition to the full time-dependent simulations, separate calculations have been performed in order to derive CO equilibrium densities. In this case, which is referred to as CE in the following, different snapshots of the time-dependent simulation sequence are used as the initial condition with the number densities derived from the gas density in the same way as done for the start model (see Sect. 4). For each grid cell the pure chemistry calculations are performed analogously to

the time-dependent treatment described in Sect. 2.2, but with the local gas temperature kept constant and without advection, until the CO number density reaches an equilibrium value $n_{\text{CO,eq}}$. Starting from an initial value $n_{\text{CO},0} = n_{\text{CO}}(t=0)$, the resulting temporal evolution of the CO number density follows in most cases the function

$$n_{\text{CO}}(t) = (n_{\text{CO},0} - n_{\text{CO,eq}}) e^{-t/t_{\text{chem}}} + n_{\text{CO,eq}}, \quad (6)$$

which is the typical solution for the differential chemistry equation (Eq. (2)). The derived profile $n_{\text{CO}}(t)$ then allows to determine the equilibrium value

$$n_{\text{CO,CE}} \equiv n_{\text{CO,eq}} = \lim_{t \rightarrow \infty} n_{\text{CO}}(t) \quad (7)$$

and the corresponding chemical timescale t_{chem} for every grid cell. In principle the assumption of instantaneous chemical equilibrium (ICE) should provide the same values, although that approach utilises chemical equilibrium constants instead of a reaction network.

For comparison, ICE number densities are calculated with the spectrum synthesis code RH (“Rybicki & Hummer”) by Uitenbroek (2001) for a number of snapshots from our time-dependent 2D model in the same way as done by Uitenbroek (2000). The results of these calculations are referred to here as UICE.

2.4. ICE and spectrum synthesis

The RH code (see Sect. 2.3) is also used for calculating spectra. We have modified this code, which by default computes the instantaneous chemical equilibrium densities for a user-defined set of molecules and their constituent atoms, to also accept the CO densities computed with CO⁵BOLD as input. The distribution over the various energy levels of the CO molecule is assumed to be in LTE, which has been shown to be a sound approximation (Ayres & Wiedemann 1989), so that the CO line opacities and line source functions are in LTE. We compute intensities in the 2142–2145 cm⁻¹ range (4.662–4.668 μm), which is observable from the ground and which contains CO lines with widely varying properties (Goorvitch 1994). Due to the non-negligible contribution of Thomson scattering to the total opacity at the wavelengths studied, we have to lambda-iterate the angle-averaged radiation field J_ν to convergence. For those computations we use the A4 angular quadrature of Carlson (1963), which has 3 rays per octant. For the intensities in the vertical direction a separate formal solution was subsequently performed using the angle-averaged radiation field J_ν from the full solution to account for the scattering contributions.

Since scattering off free electrons is an important source of opacity in higher layers of the solar atmosphere, it is necessary to use realistic electron densities. The default LTE values, obtained by solving the Saha-Boltzmann equations for all species, are definitely unrealistic in the chromosphere since there the degree of ionisation is largely decoupled from the local temperature. Instead of the default LTE values we derive electron densities from the FAL-C model (Fontenla et al. 1991) by means of interpolation of the $N_e(N_{\text{H}})$ dependence.

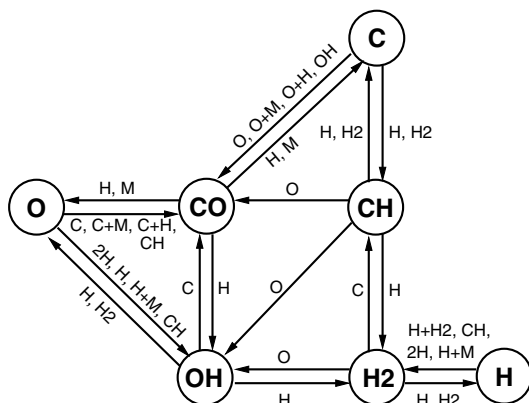


Fig. 1. Chemical reaction network. The seven chemical species (not including the representative metal) are connected via reactions which are listed in Table 1. The involved chemical species of the reactions are printed at the arrows.

In order to be consistent with the chemo-hydrodynamic calculations in this paper, the same chemical abundances have been adopted (see Sect. 4). By default, the following molecules are taken into account in RH: H_2 , H_2^+ , C_2 , N_2 , O_2 , CH , CO , CN , NH , NO , OH and H_2O . While this set is used for the spectrum synthesis, we did also a calculation with a reduced set comprised of only the molecules that are present in the chemical reaction network (see Sect. 3). The results are discussed in Sect. 6.

3. Chemical reaction network

In the present study we take into account eight chemical species: H , H_2 , C , O , CO , CH , OH and M , where M stands for a representative inert catalyst (also briefly referred to as “metal”). For the standard model (see Sect. 4) the abundance of the representative metal was set to that of helium. Strictly speaking He is not a metal but the most abundant element that can be chosen as representative catalytic element M . This way an upper limit for the influence of M is provided. The species are connected via 27 reactions (see Table 1). Ion-molecule reactions and photoreactions are excluded because, following Asensio Ramos et al. (2003), their influence on the total CO concentration is negligible for heights of ≤ 1000 km in the solar atmosphere. The chemical input data are taken from different sources¹ which are discussed below.

First, the UMIST database rate file *rate99* (Le Teuff et al. 2000) has been reduced to reactions involving the chemical species stated above.

In addition, a few termolecular² reactions are taken from the combustion database of Konnov (2000, <http://homepages.vub.ac.be/~akonnov>). Asensio Ramos et al. (2003), for example, based their chemical network entirely on the rates from this database.

¹ Note that the reference BDHL72 given here is apparently identical to BDDG72 as used by AR96.

² Termolecular: a reaction involving the simultaneous collision of three particles.

The list of reactions is further supplemented with three reactions present in Table 2 by Ayres & Rabin (1996) that are not found in UMIST (#7000, #7001, #7002). Note that their data are explicitly prepared for a gas temperature of 5000 K because of the authors’ interest in the CO reformation timescales in a previously molecule-free gas cooling below the H^- equilibrium temperature.

Some reactions are available from different sources and their reaction rate coefficients differ noticeably. Some of the rates in Konnov’s database for instance are different from those in UMIST. They differ not only in the absolute value of the rate, but also in the type of reaction (temperature dependence, activation barrier). Some others agree surprisingly well. These ambiguities demand closer examination of the chemical input data. Here we present an examination of different available sources for reaction rates included in our chemical network (see Table 1). The different data are listed in Table 2 and discussed below.

Reactions 8, 48. Since Ayres & Rabin fitted the UMIST (Millar et al. 1991, former version) reaction rate explicitly for temperatures around 5000 K, their fit is poor for gas temperatures very different from that. The newer UMIST data (Le Teuff et al. 2000) comes from the NIST database (<http://www.nist.gov>) and an accuracy of better than 25% for $300 \text{ K} < T < 2500 \text{ K}$ (8) and $297 \text{ K} < T < 3532 \text{ K}$ (48) is claimed. At high temperatures, the real rates could be an order of magnitude larger than the UMIST rate. On the other hand, Konnov’s rate for reaction #48 is very similar to that of UMIST. The assumption that both are probably based on the same experimental data supports our decision to use the UMIST reaction rate.

Reaction 14. Ayres & Rabin derived this rate from the assumption of detailed balance for reactions #14 and #67, where they calculated the CO/OH equilibrium ratio from a Saha Ansatz. The high exponent β indicates that this rate is only valid in a very narrow temperature range around 5000 K. The UMIST rate is more than one order of magnitude smaller around 5000 K. We trace the UMIST rate back to Mitchell (1984) and Westley (1980). The original work of Westley (1980) gives a ~ 5 times higher rate than Mitchell and UMIST. Since the reason for this discrepancy is unknown, we use the original rate from Westley.

Reaction 67. The source of the UMIST database is Prasad & Huntress (1980). The reaction rate did not change in UMIST between the 1991 and 1999 rate files. Konnov’s rate is ~ 5 times smaller than that of UMIST around 5000 K and has no temperature dependence (8.30×10^{-11} compared to 4.5×10^{-10}). Westley (1980) quotes a rate of 7.39×10^{-11} at 5000 K, a factor of 6 lower than UMIST. Both, Konnov’s rate and the one of Westley are valid for typical combustion temperatures, while the UMIST rate is only valid up to 300 K.

Table 1. Chemical reaction network: involved are the species H, H₂, C, O, CO, CH, OH, a representative metal (M) and photons (ν). The corresponding reaction rates are parameterised by the coefficients α , β and γ , following the UMIST standard (see Eqs. (3)–(4)). The dimension of α is cm³ s⁻¹ and cm⁶ s⁻¹ for two- and three-body reactions, respectively. β is dimensionless, γ is given in units of K. The last column gives references to the origin of the rates: UMIST: Le Teuff et al. (2000), KCD: Konnov’s combustion database (Konnov 2000), W80: Westley (1980) BDHL72: Baulch et al. (1972) BDDG76: Baulch et al. (1976); The ID numbers indicate where the reactions were found first, regardless of the final source of the coefficients which is given in the last column. An ID number less than 5000 refers to UMIST, whereas numbers 5000 and above are assigned to additional reactions found in Konnov’s database. Reactions listed by Ayres & Rabin (1996) are classified with numbers of ≥ 7000 .

ID No.	Reaction		α	β	γ [K]	Ref.
Radiative association			[cm ³ s ⁻¹]			
3681	H + C	→ CH + ν	1.00(-17)	0.00	0.0	UMIST
3683	H + O	→ OH + ν	9.90(-19)	-0.38	0.0	UMIST
3707	C + O	→ CO + ν	1.58(-17)	0.34	1297.4	UMIST
3-body association			[cm ⁶ s ⁻¹]			
5001	H + H + H ₂	→ H ₂ + H ₂	9.00(-33)	-0.60	0.0	KCD
5002	H + H + H	→ H ₂ + H	4.43(-28)	-4.00	0.0	BDHL72
7000	O + H + H	→ OH + H	1.00(-32)	0.00	0.0	BDHL72
7001	C + O + H	→ CO + H	2.14(-29)	-3.08	-2114.0	BDDG76
Species exchange			[cm ³ s ⁻¹]			
1	H + CH	→ C + H ₂	2.70(-11)	0.38	0.0	UMIST
8	H + OH	→ O + H ₂	6.99(-14)	2.80	1950.0	UMIST
14	H + CO	→ OH + C	5.75(-10)	0.50	77 755.0	W80
42	H ₂ + C	→ CH + H	6.64(-10)	0.00	11 700.0	UMIST
48	H ₂ + O	→ OH + H	3.14(-13)	2.70	3150.0	UMIST
66	C + OH	→ O + CH	2.25(-11)	0.50	14 800.0	UMIST
67	C + OH	→ CO + H	1.81(-11)	0.50	0.0	W80
102	CH + O	→ OH + C	2.52(-11)	0.00	2381.0	UMIST
104	CH + O	→ CO + H	1.02(-10)	0.00	914.0	UMIST
Collisional dissociation			[cm ³ s ⁻¹]			
4060	H + H ₂	→ H + H + H	4.67(-07)	-1.00	55 000.0	UMIST
4061	H + CH	→ C + H + H	6.00(-09)	0.00	40 200.0	UMIST
4062	H + OH	→ O + H + H	6.00(-09)	0.00	50 900.0	UMIST
4069	H ₂ + H ₂	→ H ₂ + H + H	1.00(-08)	0.00	84 100.0	UMIST
4070	H ₂ + CH	→ C + H ₂ + H	6.00(-09)	0.00	40 200.0	UMIST
4071	H ₂ + OH	→ O + H ₂ + H	6.00(-09)	0.00	50 900.0	UMIST
7002	CO + H	→ C + O + H	2.79(-03)	-3.52	128 700.0	BDDG76
Collision induced dissociation			[cm ³ s ⁻¹]			
4076	CO + M	→ O + C + M	2.79(-03)	-3.52	128 700.0	BDDG76
Catalysed termolecular reactions			[cm ⁶ s ⁻¹]			
4079	H + M + O	→ OH + M	4.33(-32)	-1.00	0.0	UMIST
5000	H + M + H	→ H ₂ + M	6.43(-33)	-1.00	0.0	KCD
4097	C + M + O	→ CO + M	2.14(-29)	-3.08	-2114.0	BDDG76

There are two reasons for choosing the Westley (1980) rate: (1) the reactions #14 and #67 form a pair of forward and backward reaction and hence the same data should be used for them. (2) This reaction rate is valid for typical combustion temperatures and hence more appropriate to the temperature range covered in our solar atmosphere simulations.

Reaction 3683. Ayres & Rabin state UMIST as source for this rate coefficient although apparently they slightly altered it. For the present chemical network the original UMIST rate is used.

Reaction 3707. After detailed examination of the original data from Dalgarno et al. (1990), and the fits by Ayres & Rabin and UMIST, we adopted the rate coefficients provided by UMIST (Le Teuff et al. 2000). The latter give the best fit in the temperature range between 2000 and 8000 K.

Reaction 4060. Again, Ayres & Rabin’s fit of the rate by Baulch et al. (1972) holds around $T \sim 5000$ K. Outside that temperature range it systematically overestimates the original data by orders of magnitude. In contrast, the UMIST rate

Table 2. Comparison of chemical data from different sources. The reaction rates are parameterised by the coefficients α , β and γ , following the UMIST standard. The dimension of α is $\text{cm}^3 \text{s}^{-1}$ and $\text{cm}^6 \text{s}^{-1}$ for two- and three-body reactions, respectively. β is dimensionless, γ is given in units of K. The sixth column gives the temperature range in K over which the reaction rate is valid and the seventh column its accuracy (following the UMIST error nomenclature, A: <25%, B: <50%, C: within a factor 2, D: within an order of magnitude, E: highly uncertain). The last column gives references to the origin of the rates: UMIST: Le Teuff et al. (2000), AR96: Ayres & Rabin (1996), KCD: Konnov's combustion database (Konnov 2000), W80: Westley (1980) BDHL72: Baulch et al. (1972) BDDG76: Baulch et al. (1976).

ID No.	Reaction	α	β	γ [K]	T range [K]	Acc.	Ref.	
1	CH + H → C + H ₂	2.70(-11)	0.38	0.0	300–2000	B	UMIST (1)	
		1.31(-10)	0.0	80.5			KCD	
8	H + OH → O + H ₂	6.99(-14)	2.80	1950.0	300–2500	A	UMIST (8)	
		3.35(-13)	1.70	0.0	~5000		AR96	
14	H + CO → OH + C	1.10(-10)	0.50	77 700.0	2590–41 000	C	UMIST (14)	
		3.21(-35)	16.20	0.0	~5000		AR96	
		5.75(-10)	0.50	77 755.0	typical T_{comb}		W80	
48	O + H ₂ → OH + H	3.14(-13)	2.7	3150.0	297–3532	A	UMIST (48)	
		2.86(-13)	1.90	0.0	~5000		AR96	
		4.10(-13)	2.7	3165.1			KCD	
67	C + OH → CO + H	1.10(-10)	0.5	0.0	10–300	C	UMIST (67)	
		1.22(-10)	0.5	0.0	~5000		AR96	
		8.30(-11)	0.0	0.0			KCD	
		1.81(-11)	0.5	0.0	typical T_{comb}		W80	
102	CH + O → C + OH	2.52(-11)	0.0	2381.0	10–6000	B	UMIST (102)	
		2.52(-11)	0.0	2380.1			KCD	
103/4	CH + O → CO + H	6.60(-11)	0.0	0.0	10–2000	A	UMIST (103)	
		1.02(-10)	0.0	914.0	2000–6000		UMIST (104)	
		6.64(-11)	0.0	0.0			KCD	
3683	H + O → OH + $h\nu$	9.90(-19)	-0.38	0.0	10–300	C	UMIST (3683)	
		9.24(-19)	-0.40	0.0	~5000		AR96	
3707	C + O → CO + $h\nu$	1.58(-17)	0.34	1297.4	300–13 900	B	UMIST (3707)	
		5.55(-18)	0.60	0.0	~5000		AR96	
4060	H + H ₂ → H + H + H	4.67(-07)	-1.00	55 000.0	1833–41 000	C	UMIST (4060)	
		3.45(-21)	6.60	0.0	~5000		AR96	
		8.86(-04)	-4.00	51 900.0	3400–5000		D	BDHL72
4062	H + OH → O + H + H	6.00(-09)	0.00	50 900.0	1696–41 000	C	UMIST (4062)	
		3.92(-26)	10.40	0.0	~5000		AR96	
4076	CO + M → O + C + M	2.86(-03)	-3.52	112 700.0	2000–10 000	B	UMIST (4076)	
		2.79(-03)	-3.52	128 700.0	7000–15 000		D	BDDG76
5000	H + H + M → H ₂ + M	6.43(-33)	-1.0	0.0			KCD	
		5.88(-33)	-1.0	0.0	1700–5000		C	BDHL72
5001	H + H + H ₂ → H ₂ + H ₂	9.00(-33)	-0.6	0.0			KCD	
		2.39(-32)	-1.0	0.0	2500–5000		D	BDHL72
5002	H + H + H → H ₂ + H	8.82(-33)	0.0	0.0			KCD	
		4.63(-28)	-4.0	0.0	~5000		AR96	
		1.83(-31)	-1.0	0.0			P83	
		4.43(-28)	-4.0	0.0	3400–5000		D	BDHL72
7000	O + H + H → OH + H	1.00(-32)	0.0	0.0	~5000		AR96	
		2.76(-33)	0.0	0.0	low.limit		E	BDHL72
		2.76(-32)	0.0	0.0	upp.limit		E	BDHL72
7001	C + O + H → CO + H	3.78(-29)	-3.50	0.0	~5000		AR96	
		2.14(-29)	-3.08	-2114.0	7000–14 000		D	BDDG76
7002	CO + H → C + O + H	1.39(-46)	22.80	0.0	~5000		AR96	
		2.79(-03)	-3.52	128 700.0	7000–15 000		D	BDDG76

deviates by not more than a factor of 3 from the original data in the range 3400 K to 5000 K. Even though the source of the UMIST fit is unknown to us, we favor it because the rate covers a larger temperature range and nicely follows the trend of the experimental data, which display a steeper gradient – steeper than the Baulch et al. (1972) formula – at temperatures below 3400 K. Baulch et al. state that their rate is only a tentative suggestion in a narrow temperature range.

Reaction 4062. The Ayres & Rabin fit is again only valid for temperatures around 5000 K. We use the UMIST data instead, because it covers the whole temperature range of interest.

Reaction 4076. The UMIST database refers to Petuchowski et al. (1989), and from there to Baulch et al. (1976) (see rate #7002). Apparently the exponent β changed in the referencing process, the factor α suffered a rounding error and the error margin has been quoted incorrectly. Hence, we use the original rate of Baulch et al. (1976).

Reaction 5002. We cannot judge the accuracy of Konnov's rate over the temperature interval $2000 \text{ K} < T < 8000 \text{ K}$, but he refers to Cohen & Westberg (1983). Palla et al. (1983) refer to a publication where Cohen is a co-author (Jacobs et al. 1967). Cohen & Westberg (1983) is newer and presents a literature review for rate constants. The difference in Baulch et al. (1972) and Konnov is the strong temperature dependence of their rates. Since Baulch et al. (1972) is a well-established and documented database – often used by UMIST as well –, we use their rate constants.

Reaction 7000. Owing to the lack of alternatives we adopt the rate by Baulch et al. (1972) although it should be regarded as only as order of magnitude estimate.

Reactions 7001, 7002. Ayres & Rabin's rate is again restricted to the 5000 K temperature range. The Baulch et al. (1976) fit assumes that H is very similar to Ar and it covers a larger temperature range, $7000 \text{ K} < T < 15000 \text{ K}$. Hence, we use the latter rate.

4. Numerical model

The two-dimensional numerical model consists of 120 by 140 grid cells each with a horizontal width of 40 km. The height of the cells is 50 km at the bottom (at $z = -1484 \text{ km}$) and smoothly decreases to 14 km for all heights above $z = -531 \text{ km}$. The upper boundary is located at 1016 km. Note that the origin of the height axis is defined by the horizontal and temporal average of Rosseland optical depth unity ($\tau = 1$). The total extent of the computational domain is thus $4800 \text{ km} \times 2500 \text{ km}$. Most numerical parameters are adopted from the recent 3D simulations by Wedemeyer et al. (2004), including the usage of grey OPAL-PHOENIX opacity (Iglesias et al. 1992; Hauschildt et al. 1997). The preliminary start model was extracted from the 3D model, too. In order to ensure relaxation

the model was advanced several simulation hours before it was supplemented with arrays for number densities of the involved chemical species. For each grid cell the same constant chemical composition is assumed. The required abundances of the atomic species are set to $[\text{C}] = 8.39$ (Asplund et al. 2005), and $[\text{O}] = 8.66$ (Asplund et al. 2004), where $[\text{H}] \equiv 12$. The initial abundances of the molecular species are set to 10^{-20} times the hydrogen density for CO, CH and C_2 , and to 10^{-4} for H_2 . The abundance of the representative metal is set equal to the helium abundance ($[\text{He}] = 11.00$) and thus provides an upper limit for the influence of the metal. The initial number densities are then directly calculated from the gas density of the final start model for the constant chemical composition described above.

For the standard model, in total 86 000 s have been calculated. The first 36 000 s are reserved to ensure a sufficient chemical relaxation of the model and are therefore excluded from analysis. The global time step, which is relevant for hydrodynamics and radiative transfer, was typically 0.2 s–0.4 s, whereas the time step for the chemistry calculations has been adjusted by the solver itself for each individual cell and global time step.

In addition to the standard model, more simulations with altered chemical network have been produced to investigate the influence of individual reactions or reaction groups on the formation of CO. All simulations covered a time span of at least 7000 s. See Sect. 5.5 for more details.

5. Results

5.1. Two-dimensional distribution

In Fig. 2 a snapshot of the 2D model after a simulation time of 70 390 s is presented. Each panel displays a different quantity as function of horizontal (x) and vertical (z) position for the time-dependent simulation (TD) but also for the equilibrium calculations CE and UICE (see Sect. 2.3), all based on the same time step. The first panel displays the gas temperature, exhibiting a few granules and intergranular downflows. In contrast to positions above granule interiors the temperature is increased above the downflows. These high-temperature regions in the middle photosphere, which form the reversed granulation pattern when seen from above (see Leenaarts & Wedemeyer-Böhm 2005, W04), are due to compression heating as result of convective overshoot. There are also high-temperature regions in the upper layers which are produced by propagating shock waves (see W04). An example for the latter can be seen in the upper part of panels a and b, outlined by the contour line for $T = 5000 \text{ K}$. Both phenomena induce spatial and temporal inhomogeneities of the thermal structure and thus provide important constraints on the CO distribution. For clarity a contour line for $T = 5000 \text{ K}$ is drawn (white line). The horizontal variations appear much smaller in terms of logarithmic gas density (panel b) which on the other hand exhibits a decrease by several orders of magnitude from bottom to top of the model.

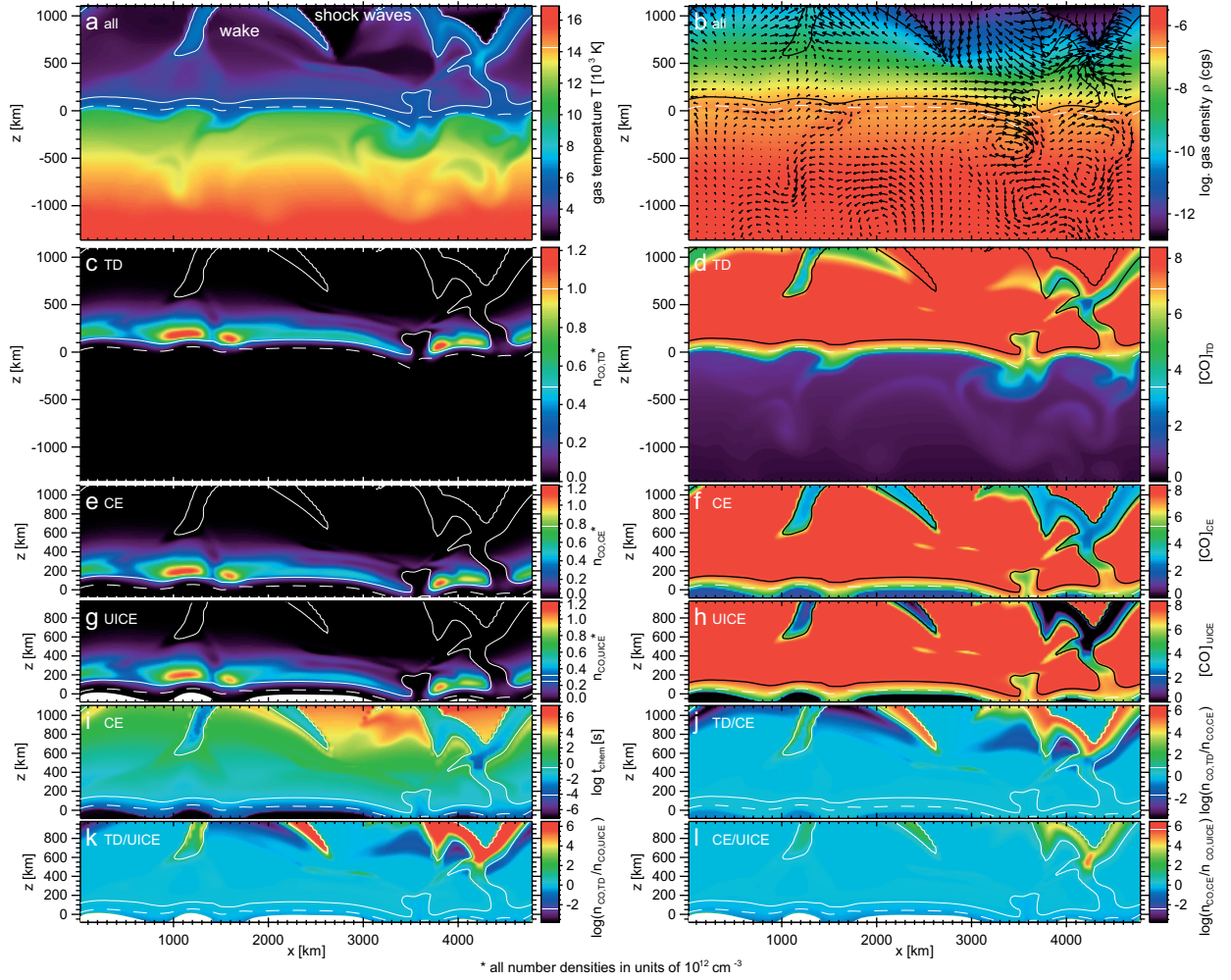


Fig. 2. Single time step of the two-dimensional model ($t = 70390$ s). The upper row shows gas temperature T **a**) and logarithmic gas density $\log \rho$ **b**), including the velocity field which is represented by arrows. The length of the arrows corresponds to the distance a fluid element travels within 15 s time (same scale as x , z -axes). The resulting CO number density $n_{\text{CO,TD}}$ is presented in panel **c**) and additionally as abundance $[\text{CO}]_{\text{TD}}$ **d**) on the usual logarithmic scale with $[\text{H}] = 12$. The third row presents the results of the equilibrium calculation (CE) for the same time step (see text for more details): CO number density $n_{\text{CO,CE}}$ **e**) and CO abundance $[\text{CO}]_{\text{CE}}$ **f**). In the next row **g**)–**h**) the corresponding results for the UICE calculation are displayed. To enable direct comparisons of the different calculations, the data ranges are the same in the second to fourth row. The chemical timescale, which has been derived from the CE simulation, is shown in panel **i**). The differences between the three cases are plotted in terms of logarithmic fractions for the pairs TD/CE, TD/UICE, and CE/UICE in panels **j**)–**l**), respectively. In the lowest row all cells with temperatures above 9000 K appear white since those are excluded in the UICE calculations. The corresponding color/greyscale-coding is shown next to each panel. The curves mark the height of average Rosseland optical depth unity (dashed) and $T = 5000$ K (solid). The solid curves clearly outline propagating shock waves in the model chromosphere. Note that for the cases CE and UICE only the upper part of the model is displayed whereas the whole height extent is shown in the upper panels for the time-dependent simulation.

The structuring in temperature and density has direct influence on the CO number density $n_{\text{CO,TD}}$ in panel **c**) which is alternatively presented as CO abundance ($[\text{CO}]$, panel **d**). CO is located mostly within a thin layer in the middle photosphere and closely follows changes of the gas temperature (see panel **a**), filling the cool interiors of the reversed granulation pattern. Due to the steep density gradient in the atmosphere the CO number density decreases rapidly with height. Nevertheless, the relative number of CO molecules remains high in the upper layers as can be seen from the CO abundance, which is defined as the ratio of CO particles to the total number of hydrogen atoms (including those bound in molecules) on the commonly

used logarithmic scale with $[\text{H}] \equiv 12$. Here, $[\text{CO}]$ is typically close to a value of 8.3 but it is strongly reduced at positions where the gas temperature exceeds ~ 5000 K (indicated by the white lines). This is true for the convection zone below the photosphere but also for the propagating shock waves which are a ubiquitous phenomenon in the upper layers. For the latter, the abundance reveals a shift of the correlation between temperature and CO density which is otherwise strong in the layers below. $[\text{CO}]$ is still high at the fronts of the displayed shock waves, but it is not restored immediately in the wake. This is clear evidence that CO does not react instantaneously to thermal changes but rather on a chemical timescale (shown in

panel i, see Sects. 5.2 and 5.4 for more details) which is longer than the dynamic timescale due to wave propagation. The dynamic behaviour and in particular the almost instantaneous reaction of the CO number density to temperature changes in the photosphere can be seen in an animation provided as online material³.

The results of the corresponding equilibrium calculations CE and UICE are shown in panels e, f and g, h, respectively. The logarithmic ratios of the CO number densities of the different cases can be seen in panels j–l (j: TD/CE, k: TD/UICE, l: CE/UICE). Note that for UICE temperatures greater than 9000 K automatically result in a zero CO number density. Those cells are blanked in the plots.

The CE case is very similar to the time-dependent result almost everywhere in the photosphere but differs strongly in chromospheric shock waves and their wakes. Although the [CO] abundance is strongly reduced directly at the wave crest in both cases, the time-dependent calculations still result in a higher density at the front of the propagating wave and in a lower one in the wake. This effect is caused by the essential but wrong assumption in CE that chemical equilibrium is reached before the gas temperature can change, analogous to the ICE assumption. Hence, CO equilibrium number density and local gas temperature do correlate strongly here, in contrast to the time-dependent simulation which takes into account finite chemical timescales in combination with the fast propagation of thermal inhomogeneities. In the latter (more realistic) case CO is only gradually dissociated when a hot wave arrives and does not form again instantaneously after the passage. The equilibrium approach by its nature cannot take into account this behaviour.

The case UICE yields a very similar picture but with somewhat smaller CO number density. Similar to CE, the deviations from the time-dependent model are small in the photosphere but become significant in the chromospheric shock waves. Finally, we compare CE and UICE: Deviations are very small in the photosphere but still get large at high temperatures in the centres of chromospheric shock waves. This remaining discrepancy must be attributed to differences in chemical input data for which equilibrium constants are used for UICE but the chemical reaction network for CE. In particular the reaction rate coefficients must be considered as potential source of errors since they are mostly defined for very limited temperature ranges only (see Table 2). At the crests of shock waves, where the largest discrepancies are found, the temperatures are high and thus exceed the stated range for many reactions.

5.2. Dependence on gas density and temperature

For a sample of the 139 snapshots available both for the TD and the CE calculations, different quantities are calculated as function of gas density and temperature. All grid cells in this sample – regardless of their spatial and temporal position – are sorted into discrete bins for logarithmic gas density $\log \rho$ and gas temperature T . The number of matching cells for each bin (Fig. 3a) is highest close to the average stratification (see dashed line) but much smaller for small densities and high

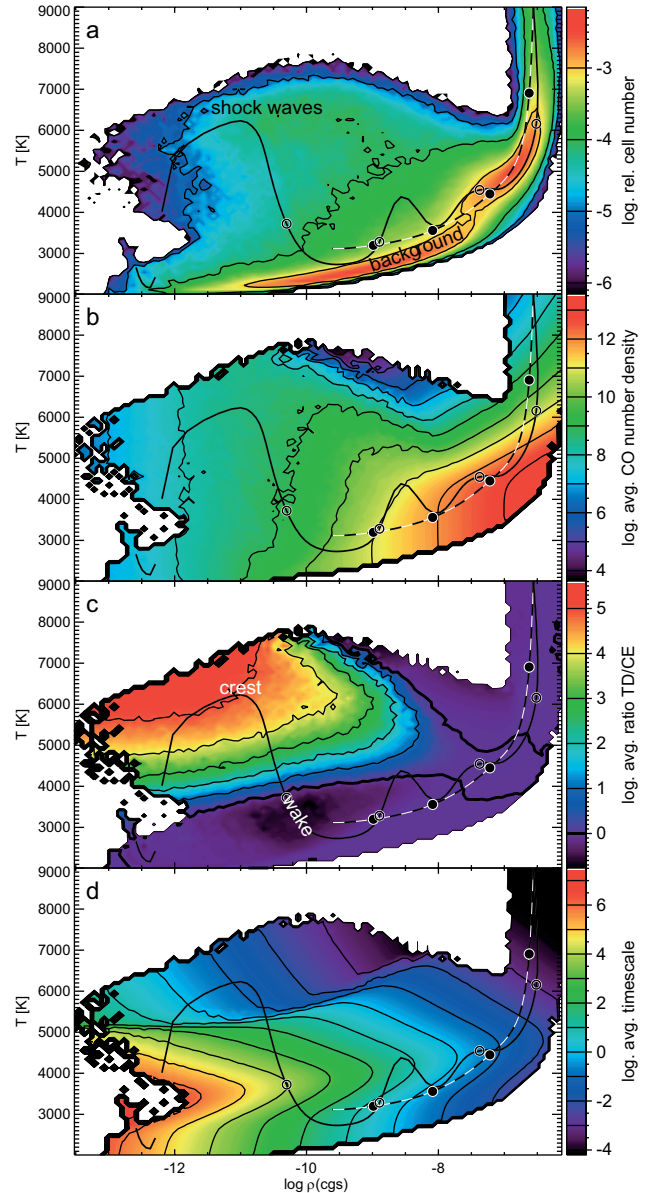


Fig. 3. Quantities as functions of logarithmic gas density and gas temperature for a sample of 139 snapshots: **a)** log. relative number of cells, **b)** log. averaged CO number density of TD case ($\log \langle n_{\text{CO,TD}} \rangle$), **c)** log. averaged ratio of TD and CE cases ($\log \langle n_{\text{CO,TD}} / n_{\text{CO,CE}} \rangle$), **d)** log. averaged chemical timescale (CE); Contours and colors/grey scales are explained in the legend right next to each panel. The thick dashed line represents the horizontally and temporally averaged stratification of the whole sequence, whereas the thick triple-dot-dashed line marks a vertical column in the representative snapshot (see Fig. 2) at $x = 2380$ km, crossing a prominent shock wave. The circles mark heights of $z = 250$ km, 500 km and 750 km, respectively.

temperatures in the upper left part of the plot which represents the domain of chromospheric shock waves. Furthermore, a gradual bifurcation can be seen with a cool background close to the average stratification and a hot component due to shock waves above (see also W04). The upper right part of the distribution corresponds to the top of the convection zone.

³ Additional material can be found at EDP.

Panel b reveals the clear tendency of CO being concentrated where the temperatures are low and gas densities are high. These conditions are best realised in the cooler regions above granule interiors in the low and middle photosphere of the model atmosphere. This causes the absolute number density to correlate best with a temperature of ~ 4400 K.

More remarkable is the difference between TD and CE, which exhibits a significant pattern in panel c. While the ratio of the corresponding CO number densities is small close to the average stratification, large values are the rule in the hot shock wave domain. The deviations in the wakes, which are due to a finite timescale on which the dissociated CO builds up again, appear as an “eye” around $\log \rho \sim -10$ and $T \sim 3000$ K. The triple-dot-dashed line represents a column in the exemplary model snapshot at $x = 2380$ km (see Fig. 2) which crosses a prominent shock wave. Consequently, this line traverses the “eye” and the shock wave domain in the $(\log \rho, T)$ -plot.

Finally, the chemical timescale (Fig. 3d) derived in the CE calculations shows: (i) The timescale grows strongly with decreasing gas density. (ii) The skew in the shock wave domain indicates that the timescales there are much shorter due to a reduced final equilibrium concentration. (iii) At a given gas density (and thus at a given geometrical height) a large range of values is present, making it difficult to define a meaningful average (see also Sect. 5.4).

5.3. Height distribution

Averaging the CO number density horizontally and in time over a time span of 50 000 s on the geometric height scale of the standard model results in the height distribution displayed in Fig. 4. It shows a prominent peak of $\max(\langle n_{\text{CO}}(z) \rangle_{x,t}) = 2.81 \times 10^{12} \text{ cm}^{-3}$ at a height of $z = 197$ km. Note that averaging on the Rosseland optical depth scale leads to a somewhat higher maximum of $\max(\langle n_{\text{CO}}(\tau) \rangle_{x,t}) = 3.68 \times 10^{12} \text{ cm}^{-3}$ at an optical depth $\log \tau = -1.17$ which on average corresponds to a geometrical height of $z = 217$ km. The corresponding average abundance increases rapidly in the photosphere until a value of ~ 8.3 is reached at the bottom of chromosphere where it stays roughly constant. For the example time step, which is also shown in Fig. 4, the horizontally averaged CO distribution is very close to the corresponding equilibrium values (CE) but starts to deviate increasingly above the photosphere (see thin solid and dot-dashed lines). This result is expected since deviations mostly occur in the hot shock waves which become prominent usually in the low chromosphere and above (see Fig. 2j). In the photosphere the conditions are suitable for equilibrium. The same behaviour is found for the UICE case which perfectly matches the average CE profile for the example time step. However, the maximum is smaller by a factor of 0.86 in the UICE case compared to TD and CE (see Fig. 4).

5.4. Chemical timescales

Already the fact that the CO number density closely outlines the hotter regions in the low and middle photosphere (see Fig. 2) indicates that the chemical timescales there are short

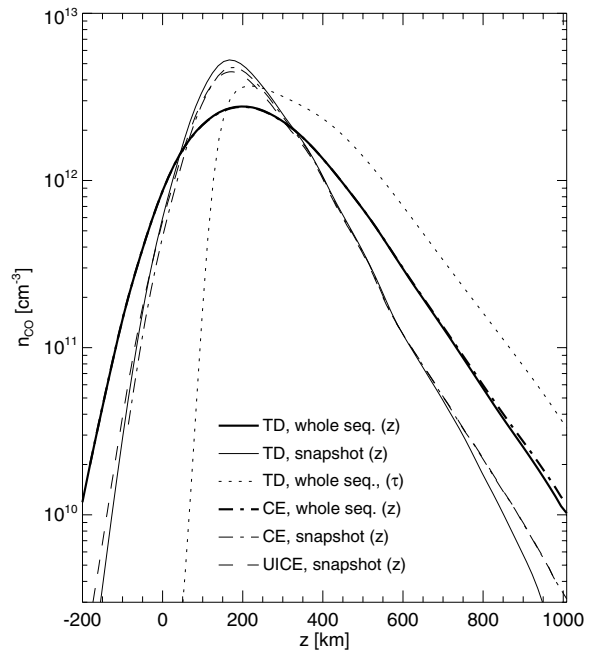


Fig. 4. Average CO number density as function of geometrical height for the whole time-dependent simulation sequence (thick solid) and for the exemplary time step shown in Fig. 2 (thin solid). The results of the equilibrium calculations (CE) are displayed for the whole sequence (thick dot-dashed) and for the exemplary time step (thin dot-dashed), and for the UICE calculation (thin dashed, snapshot only). The dotted line represents the average for the whole sequence averaged on the Rosseland optical depth scale.

compared to the timescales on which the atmospheric conditions change. Strictly speaking, chemical equilibrium refers to a given thermodynamic state of the atmosphere, for instance expressed in terms of gas temperature and particle densities. To reach equilibrium it is thus essential that these quantities stay constant. But under continuously varying conditions the chemical equilibrium can only be realised if the corresponding timescale is shorter than the dynamic one. Otherwise the concept of chemical timescales loses its meaning.

Nevertheless, chemical time scales are in general very helpful since they allow one to estimate the importance of individual reactions or reaction groups and, furthermore, are needed to decide whether the assumption of instantaneous chemical equilibrium is valid or time-dependent simulations are necessary.

In principle the chemical time scale of a reaction is given by its inverse rate (see, e.g., Herbst & Klemperer 1973; Ayres & Rabin 1996), for instance,

$$t_{\text{chem}} = (k_{7002} n_{\text{H}})^{-1} \quad (8)$$

for the two-body CO dissociating reaction #7002 (see Table 1). The required equilibrium number densities of the involved species can be estimated for individual reactions/reaction pairs in the way shown by Herbst & Klemperer (1973) and Ayres & Rabin (1996) but are difficult to obtain in the present case of a complex chemical reaction network. Already the assumption of equilibrium number densities for the involved species is questionable since those species themselves undergo a chemical evolution. Each reaction, which e.g. forms CO, not only

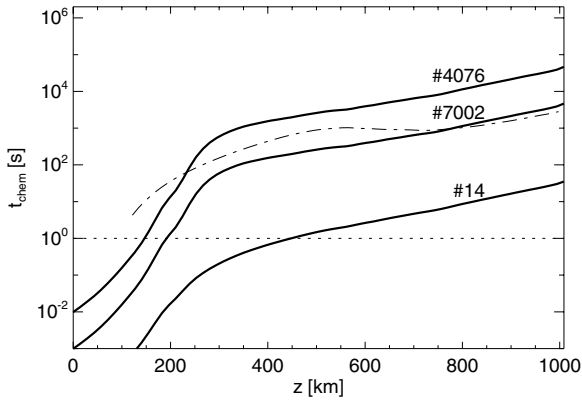


Fig. 5. Chemical timescales calculated from the average rates for the three dissociating reactions #14, #4076 and #7002 (thick solid) and the result from the time-dependent calculation in W04 (thin dot-dashed).

depends on the local gas temperature and thus on the corresponding rate coefficient k but also on the number densities of the required reactants. If now one of the involved species is not available in sufficient amounts, owing to another less efficient reaction producing this species, this “bottle-neck” reduces the total effectiveness of this formation channel. A chemical timescale of an individual reaction is thus only of limited scope under non-equilibrium conditions and rather must be seen in the context of the whole reaction network.

The CE calculations described in Sect. 2.3 take into account the chemical evolution of the whole reaction network and allow us to derive total effective chemical timescales and corresponding CO equilibrium densities. For the example the resulting CE timescales are shown in Fig. 2i, while the dependence on logarithmic gas density and temperature is displayed in Fig. 3d. These two figures show that a high temperature results in a low final CO number density and a related short timescale, whereas low temperatures lead to long timescales. Hence, the strong thermal inhomogeneities of the model atmosphere result in a very large spread of timescales, covering many magnitudes, which makes it hard to define a representative average.

Instead, we present average timescales for the three CO dissociating reactions #14, #4076 and #7002 in Fig. 5 in order to quantify the relative contribution of these reactions. For this the reaction rates are calculated for each grid cell for snapshots with a cadence of 100 s. After averaging temporally and horizontally for each reaction independently, the inverse average rates give the chemical timescales displayed in the figure. Obviously, the time scale for reaction #14 is much shorter than those for the other two. Reaction #7002 is typically two orders of magnitude slower, reaction #4076 even around three. Consequently the total chemical timescale, given by the inverse sum of the rates of the three destruction reactions, is governed by reaction 14 alone. At a height of $z = 646$ km, where the average mass density is $\langle \rho \rangle_{x,t} = 10^{15} \text{ g cm}^{-3}$, the chemical timescale for reaction #14 is only ~ 3 s which corresponds to a gas temperature of ~ 4900 K. This can be compared to 0.7 s for the rate coefficients given by Ayres & Rabin (1996) (see Table 2). However, also for this particular column density a large range of temperatures and related timescales is found.

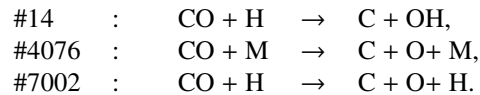
Hence, the average numbers should be considered as rough estimates only.

The timescale for reaction #7002 deviates to some extent from the result in W04. This is mainly due to the fact that the reaction coefficients by Ayres & Rabin (1996) were used in W04 instead of those by Baulch et al. (1976) as done in this work. The two parameterisations only lead to similar reaction rates close to 5000 K and deviate otherwise. Nevertheless the average timescales agree quite well above $z \sim 700$ km.

5.5. Importance of individual reactions

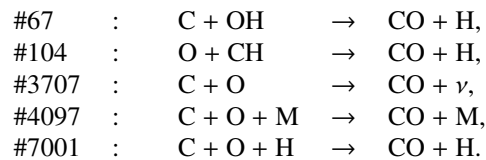
Next to the distribution of CO the relative contribution of individual reactions also is of great interest. This information allows us to reduce the chemical reaction network as much as possible by excluding irrelevant reactions and thus increasing computational performance. One also gets to know which reactions are most important.

In our reaction network three reactions dissociate carbon monoxide:



As we showed in Sect. 5.4 the species exchange reaction #14 is by far the most efficient dissociation channel whereas #7002 and #4076 only contribute 10^{-2} and 10^{-3} in the low photosphere and 10^{-3} and 10^{-4} above, respectively, in terms of number of dissociated molecules per time.

There are five reactions that form CO:



Again, the species exchange reactions are the most effective ones under the conditions of the solar atmosphere. These reactions, namely #67 (via OH) and #104 (via CH) have similar rates, although the formation channel via CH seems to be slightly faster for temperatures below ~ 7500 K. The other reactions, including the direct radiative association (#3707), are negligible compared to the CH and OH channels.

Not only the reaction rates but the product of the rates and the number densities of the involved species are crucial for the change of the CO number density (see Sect. 2.1). The average abundance of CH has a maximum of ~ 4.9 in the photosphere and decreases above to only ~ 3.9 , while OH is on average one to two magnitudes more abundant for all atmospheric heights, ranging from $[\text{OH}] \sim 5.0$ at the bottom of the photosphere to $[\text{OH}] \sim 7.6$ in the low chromosphere. Hence, the formation channel via OH is much more important than the CH channel due to the higher number density of the required reactant.

In order to investigate this matter in more detail, additional runs⁴ with different networks have been carried out. In all cases we started from the default network presented in Table 1 and Fig. 1. In case A all reactions involving CH are eliminated. The relative distribution does not change significantly. The absolute values are on average only reduced by $\sim 9\%$ compared to the results with the full network. The same is true for the peak of the horizontally and temporally averaged CO number density (see Table 3). For case B also the reactions #3707, #4076, #4097, #7001 and #7002 are removed. In the remaining network carbon monoxide can only be formed or destroyed via OH, i.e. reactions #14 and #67. The resulting CO number density closely matches that of the previous case outside small regions with extreme temperatures. In contrast, the exclusion of OH (case C) produces on average a factor of ~ 3 more CO at most positions. In chromospheric shock waves, however, n_{CO} is not as strongly reduced as in the case with the full network. Carbon monoxide is nevertheless concentrated mostly in the cool areas of reversed granulation in the middle photosphere. Excluding both OH and CH (case D) results in a generally lower CO density, where the largest differences are found in shock waves. Again, as in case C, CO is not as strongly reduced as for the full network. Note that the reduced network is separated into two isolated parts, namely $\text{H} \leftrightarrow \text{H}_2$ and $\text{C} \leftrightarrow \text{CO} \leftrightarrow \text{O}$. The simulation run without the four reactions involving the representative metal (case E) leads almost to the same results as the standard case. For temperatures below ~ 6000 K the difference in n_{CO} between the simulations with and without metal is less than one percent and it increases only slightly to a maximum of ~ 2 percent for higher temperatures. We thus conclude that the adopted catalytic reactions and also the abundance of the representative metal are of minor importance here. Finally, the network in case F comprises only the two reactions for radiative association (#3707) and collisional dissociation (#7002). The same pair was used in W04 (see also Ayres & Rabin 1996) but here we use the reaction coefficients chosen in this work (see Sect. 3). The absolute CO number density is on average roughly one order of magnitude lower than the standard case. The relative distribution stays similar, except for the upper layers. There the simple reaction pair produces a smaller relative CO concentration that, however, is not as strongly reduced in shock waves as it is in the case of the full network. This is in line with the calculations in W04 for which the fraction of all carbon atoms bound in carbon monoxide was only $\sim 10\%$. This compares to an average fraction of 80% derived with the full network.

The ratio of the peak of the average CO number density of the different cases and the default network in Table 3 can be used to summarise the aforementioned results. Catalytic reactions are negligible (case A). The CH channel is only of secondary importance but should not be omitted (case A). In contrast #3707, #4076, #4097, #7001 and #7002, including radiative association and collisional dissociation (case F), can be neglected (see case C compared to case B). Most important is

Table 3. Comparison of simulations with different chemical reaction networks (case A–F, see text) and the full network (REF). Given are the number of remaining reactions n_{reac} , absolute value ($\max(\langle n_{\text{CO}} \rangle)$) and height (z_{max}) of the maximum of the averaged CO number density, the ratio of the peak number density and the maximum value of the standard case ($\delta n_{\text{CO}} = \max(\langle n_{\text{CO}} \rangle) / \max(\langle n_{\text{CO}} \rangle_{\text{ref}}$), and the gas temperature T_{mc} that correlates best with CO number density.

case	n_{reac}	$\max(\langle n_{\text{CO}} \rangle)$ [10^{12} cm^{-3}]	z_{max} [km]	δn_{CO}	T_{mc} [K]
REF (all)	27	3.46	171	1.00	4400
A (no CH)	19	3.15	185	0.91	4400
B (no CH +5)	14	3.15	185	0.91	4400
C (no OH)	16	10.88	101	3.15	5200
D (no CH, no OH)	10	2.37	129	0.69	4700
E (no M)	23	3.45	171	0.99	4400
F (#3707, #7002)	2	0.27	157	0.08	4600

the channel via OH (case B). Excluding it from the network (case C) produces fundamentally different results.

5.6. CO spectrum synthesis

A sample of 50 snapshots with constant cadence from the time-dependent 2D simulation sequence was used as input for the spectrum synthesis code RH by Uitenbroek (see Sect. 2.4). For all snapshots a spectrum for the same wavelength range near $4.7 \mu\text{m}$ was calculated for disk-centre ($\mu = 1.0$). In Fig. 6 the horizontal and temporal average of these spectra is shown in comparison with data from the third version of the Atmospheric Trace Molecule Spectroscopy (ATMOS3) atlas (Farmer 1994; Farmer et al. 1989, <http://remus.jpl.nasa.gov/atmos>). The ATMOS3 data were scaled to match the continuum intensity of the averaged synthetic spectrum.

Since the CO number density of the time-dependent and the ICE approach closely match in the line-forming layers, also the resulting spectra agree almost perfectly. But both exhibit much deeper line cores than seen in the ATMOS3 data, similar to the results by Uitenbroek (2000, see his Fig. 11). Owing to the dynamics, which tend to be too strong in 2D simulations, and the small model extent, the CO number density, the resulting depth of the absorption lines, and also the continuum intensity vary significantly. Although there are times and positions that can produce a better fit than the average shown here, the chosen number of 50 snapshots might still be too small to make up a representative sample. This is also implied by the fact that the average continuum intensity level only corresponds to a brightness temperature of 5400 K. The sample is obviously not perfectly representative but rather is too cold. This would produce too much CO and consequently too deep line cores. Lines with low excitation potential seem to deviate more from the ATLAS data than lines with higher excitation potential. Given that low excitation lines are formed further up in the atmosphere, this trend could point out too much CO in the higher layers. On the other hand, the spectra with

⁴ Simulation snapshots for the different cases are provided as online material.

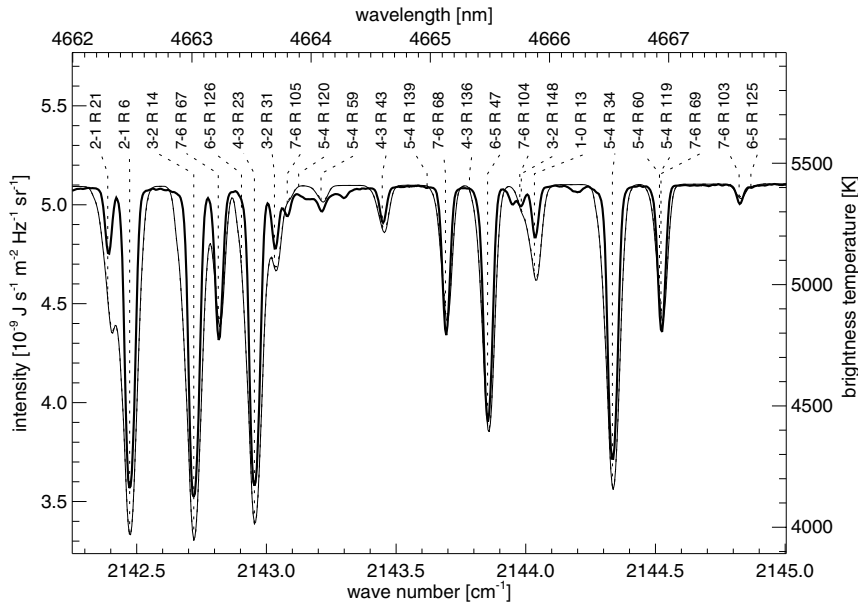


Fig. 6. Spectra near $\lambda = 4.7 \mu\text{m}$ with fundamental vibration rotation lines of carbon monoxide (R branch): average synthetic spectra with CO densities from time-dependent 2D model (thin solid) compared to ATMOS3 data (thick solid). Note that the UICE calculation exactly coincides with the time-dependent case.

ICE assumption show exactly the same behaviour, in contrast to Uitenbroek (2000).

6. Discussion

Spatial distribution. As stated in Sect. 5.1 we find the maximum of the average CO height-distribution to be $2.8 \times 10^{12} \text{ cm}^{-3}$ at $z = 197 \text{ km}$. Despite differences in the assumed rate coefficients, this is in line with the work by Asensio Ramos et al. (2003) who find, judging from their Fig. 2, a peak value of $\sim 3 \times 10^{12} \text{ cm}^{-3}$ at $z \approx 100 \text{ km}$. Uitenbroek (2000) does not provide a horizontal average but the spatial CO distribution in a two-dimensional cut through the adopted model (see his Fig. 9). There, the highest values are between $\sim 3 \times 10^{12} \text{ cm}^{-3}$ and $\sim 10^{13} \text{ cm}^{-3}$ in the low and middle photosphere. As well as these high values, which are mostly found above granule interiors, smaller CO concentrations are present above intergranular lanes. The horizontal average of the distribution is thus in line with the results of this work, concerning the maximum values as well as their spatial distribution. Furthermore, the findings also agree with Ayres (1981), who finds $\tau_{500} \leq 10^{-2}$ as the upper limit for the peak of the CO distribution. This optical depth corresponds to a geometrical height of $z = 365 \text{ km}$ in our model and is indeed higher than the peak found here. Also the fact that CO is mostly located in the cool regions of the reversed granulation pattern matches the observed pattern. Uitenbroek (2000) reported on spectroheliograms in the cores of strong CO lines near $\lambda = 4.7 \mu\text{m}$ that exhibit dark areas as small as $1''$, lasting for several minutes, surrounded by bright network-like rims (see also Uitenbroek et al. 1994). The same is not only seen in the two-dimensional model presented here but even more clearly in early results from 3D simulations that are currently in progress.

The finding that the bulk of CO is located in the photosphere also fulfills other indirect constraints like the presence of 5 min oscillations. Such prominent intensity oscillations were discovered by Noyes & Hall (1972b) in the core of the

3–2 R14 CO line in the fundamental vibration-rotation bands ($\Delta V = 1$) near a wavelength of $\lambda = 4.7 \mu\text{m}$ (see also Ayres & Brault 1990). This line should be formed in the high photosphere (Noyes & Hall 1972a), where 5 min oscillations can clearly be detected.

On the other hand, the differences between the synthetic spectra and the observed ATMOS3 data might indicate that the model still exhibits too much CO – at least in the upper layers. One possible cause might be a too simple treatment of the radiative transfer in the chromosphere which is still treated frequency-independently (grey) and under the assumption of local thermodynamic equilibrium (LTE). A small error in the resulting gas temperature can generate significant changes in CO number density. Another possibly more severe source of too high CO number densities might come from incorrect or uncertain rate coefficients. However, in order to resolve these possibilities a larger and thus more significant set of synthetic spectra is needed.

Necessary modelling. An important result is that CO is mostly concentrated within the cool regions of the reversed granulation pattern. Hence, particular care should be taken in modelling the corresponding mid-photospheric layers. Although the basic features are matched, the atmospheric structure in a small two-dimensional model suffers from the vast dynamics which are usually exaggerated in 2D simulations compared to 3D. Consequently, we strongly recommend use of three-dimensional models like the one described in W04 which has been proven to produce a very realistic reversed granulation pattern (Leenaarts & Wedemeyer-Böhm 2005). A 3D model provides much better statistics which are crucial for the synthesis of meaningful spectra (see Sect. 5.6). We expect many results to remain qualitatively the same, e.g., the dependence on temperature and gas density (Sect. 5.2), the relative contribution of individual reactions (Sect. 5.5), and the differences between ICE and time-dependent approach. In contrast the average stratification and fluctuations of temperature and

CO number density may be slightly different in 3D compared to 2D but still the qualitative picture should be the same.

Another point concerns the radiative transfer which is treated frequency-independently (“grey”) in the simulations presented here. For comparison we calculate a short sequence with a non-grey multi-group scheme (cf. Ludwig 1992; Wedemeyer 2003). The differences in gas temperature and in CO number density are still small in the middle photosphere where the bulk of CO is found. In contrast, there are significant differences in the chromosphere. The temperature fluctuations are much smaller there in the non-grey case. As a result the CO number densities of the grey and the non-grey simulation deviate most in the hottest parts of chromospheric shock waves. While the multi-group approach produces a more realistic thermal structure of the photosphere, the situation is less clear in case of the chromosphere. There, neither the grey nor the multi-group LTE approach is appropriate. Rather a frequency-dependent non-LTE radiative transfer is required which is unfortunately not available yet. Nevertheless, the grey approach is preferable since it produces results (e.g., shock peak temperatures) that surprisingly agree better with other works (e.g. Carlsson & Stein 1995; Skartlien 1998) than those obtained with the multi-group scheme (see W04 for a detailed discussion). But the modelling of chromospheric radiative transfer still remains a major weakness and thus needs to be improved in future.

For the modelling of the number densities of the chemical species the ICE assumption seems to be valid in the photosphere where chemical timescales are mostly much shorter than the dynamical one so that advection and non-equilibrium effects can be neglected there – a result already mentioned by Asensio Ramos et al. (2003). This is also implied by the agreement of the CO distribution with the results of Uitenbroek (2000). Hence, no time-dependent calculations seem to be necessary for the *photosphere* which contains by far the largest absolute amount of carbon monoxide. In contrast, the ICE assumption fails close to shock waves in the *chromosphere* where a time-dependent treatment is mandatory.

The remaining discrepancies in CO equilibrium densities between the calculations based on the reaction network (CE) and the ICE approach (UICE) can be attributed to differences in chemical input data that are equilibrium constants for UICE but rate coefficients in the reaction network. In particular the limited temperature range for which many rates are defined might explain why the largest deviations are found at the hot crests of the chromospheric shock waves. There gas temperatures often exceed the stated range for many reactions.

Chemical reactions. A thorough analysis of chemical reaction coefficients and additional simulations with altered chemical networks leads us to the conclusion that OH is the most important agent for forming and dissociating carbon monoxide whereas the CH branch contributes much less – a result already suggested by Ayres & Rabin (1996). In contrast, the reaction pair composed of radiative association and collisional dissociation cannot reproduce the observed CO distribution. Catalytic

reactions involving a representative metal are negligible even if it is assumed to be as abundant as helium.

Unlike Asensio Ramos et al. (2003) we did not account for nitrogen chemistry in our reaction network. In order to check the possible consequences of the exclusion of nitrogen, we directly compared ICE number densities calculated with the RH code for the exemplary time step (see Sect. 5) for two different sets of molecules: the complete default set (see Sect. 2.4) and a set that only included those molecules that are also part of the reaction network used for our time-dependent simulations. Hence, both sets differ by the following molecules: H_2^+ , C_2 , N_2 , O_2 , CN , NH , NO and H_2O . This includes all molecules used for nitrogen chemistry by Asensio Ramos et al. The differences in CO number density between the two cases are negligible in the atmosphere, in particular at the heights where the bulk of CO is present. In contrast, the reduced set resulted in a CO number density lower by up to five orders of magnitude at the hot centres of chromospheric shock waves but there only little CO is found. Moreover, the average CO height distribution of our time-dependent simulation is very similar to that of Asensio Ramos and co-workers. We thus conclude that nitrogen chemistry may be negligible for the formation of CO in the solar atmosphere – at least outside the problematic hot centres of chromospheric shock waves.

Chemical timescales. The rates and the corresponding timescales span a range of several orders of magnitude, making it difficult to define a meaningful average. The results presented here should thus serve as a first-order estimate only.

7. Conclusions

The presented 2D radiation chemo-hydrodynamic simulations produce a spatial distribution of carbon monoxide that agrees well with earlier theoretical work and also with observations. The synthetic spectra match reasonably well if one considers the large fluctuations that are unavoidable in the case of such a small-size two-dimensional model. More accurate results can be expected from a 3D simulation which is currently in progress. The presented model proved that CO is mostly located in the cool regions of the reversed granulation pattern at mid-photospheric heights. Some effort was spent in making the applied chemical reaction network as realistic as possible on the basis of the available chemical input data whose quality is quite poor in some cases. Hydroxide (OH) was found to be the most important ingredient for the formation and destruction of carbon monoxide.

The presented comparison between the time-dependent simulation and the corresponding instantaneous chemical equilibrium (ICE) case shows that significant deviations occur only near hot shock waves in the solar chromosphere. Hence, ICE is a valid assumption for the photosphere that allows us to treat CO in a simple way in simulations that do not extend beyond the photosphere. In contrast, ICE fails in and close to propagating high-temperature regions at chromospheric densities. Rather, a time-dependent treatment, as presented in this work, is mandatory for realistic simulations of the solar chromosphere.

We take the agreement of our results with other works as demonstration of the validity of the approximations and algorithms of the upgraded code CO⁵BOLD in the case of CO in the solar atmosphere. It now can be used for a wide range of applications for other stellar types and other chemical reaction networks.

Acknowledgements. T. Ayres, A. Konnov and T. J. Millar gave helpful advice concerning chemical reaction rates. We thank T. Ayres for valuable comments and H. Uitenbroek for providing his RH code. S.W. acknowledges support by the *Deutsche Forschungsgemeinschaft (DFG)*, project Ste 615/5.

References

- Asensio Ramos, A., Trujillo Bueno, J., Carlsson, M., & Cernicharo, J. 2003, *ApJ*, 588, L61
- Asplund, M., Grevesse, N., Sauval, A. J., Allende Prieto, C., & Kiselman, D. 2004, *A&A*, 417, 751
- Asplund, M., Grevesse, N., Sauval, A. J., Allende Prieto, C., & Blomme, R. 2005, *A&A*, 431, 693
- Ayres, T. R. 1981, *ApJ*, 244, 1064
- Ayres, T. R. 1991, *An Infrared Perspective on Chromospheres*, ed. P. Ulmschneider, E. Priest, & R. Rosner (Heidelberg: Mechanisms of Chromospheric and Coronal Heating, Springer-Verlag), 228
- Ayres, T. R. 2002, *ApJ*, 575, 1104
- Ayres, T. R. 2004, in *ESA SP-547, SOHO 13 Waves, Oscillations and Small-Scale Transients Events in the Solar Atmosphere, Joint View from SOHO and TRACE*, 119
- Ayres, T. R., & Brault, J. W. 1990, *ApJ*, 363, 705
- Ayres, T. R., & Rabin, D. 1996, *ApJ*, 460, 1042 (AR96)
- Ayres, T. R., & Testerman, L. 1981, *ApJ*, 245, 1124
- Ayres, T. R., Testerman, L., & Brault, J. W. 1986, *ApJ*, 304, 542
- Ayres, T. R., & Wiedemann, G. R. 1989, *ApJ*, 338, 1033
- Baulch, D., Drysdale, D., Duxbury, J., & Grant, S. 1976, *Evaluated Kinetic Data for High Temperature Reactions*, Vol. 3 (Butterworth) (BDDG76)
- Baulch, D., Drysdale, D., Horne, D., & Lloyd, A. 1972, *Evaluated Kinetic Data for High Temperature Reactions*, Vol. 1 (Butterworth) (BDHL72)
- Baulch, D. L., Cobos, C. J., Cox, R. A., et al. 1992, *J. Phys. Chem. Ref. Data*, 21, 411
- Brown, P., Byrne, G., & Hindmarsh, A. 1989, *SIAM J. Sci. Stat. Comp.*, 10, 1038
- Carlson, B. G. 1963, in *Methods in Computational Physics*, ed. B. Alder, S. Fernbach, & M. Rotenberg, 1, 1
- Carlsson, M., & Stein, R. F. 1995, *ApJ*, 440, L29
- Carlsson, M., & Stein, R. F. 1997, *ApJ*, 481, 500
- Carlsson, M., & Stein, R. F. 2002, *ApJ*, 572, 626
- Cohen, N., & Westberg, K. R. 1983, *J. Phys. Chem. Ref. Data*, 12, 531
- Dalgarno, A., Du, M. L., & You, J. H. 1990, *ApJ*, 349, 675
- Farmer, C. B. 1994, in *Infrared Solar Physics*, IAU Symp., 154, 511
- Farmer, C. B., Norton, R. H., & Geller, M. 1989, *A High-Resolution Atlas of the Infrared Spectrum of the Sun and Earth Atmosphere from Space*, (Washington, DC: NASA, Scientific and Technical Information Service, 1989–1992), Vol. 1
- Fontenla, J. M., Avrett, E. H., & Loeser, R. 1991, *ApJ*, 377, 712
- Freytag, B., Steffen, M., & Dorch, B. 2002, *Astron. Nachr.*, 323, 213
- Goorvitch, D. 1994, *ApJS*, 95, 535
- Hauschildt, P. H., Baron, E., & Allard, F. 1997, *ApJ*, 483, 390
- Herbst, E., & Klemperer, W. 1973, *ApJ*, 185, 505
- Iglesias, C. A., Rogers, F. J., & Wilson, B. G. 1992, *ApJ*, 397, 717
- Jacobs, T. A., Giedt, R. R., & Cohen, N. 1967, *J. Chem. Phys.*, 47, 54
- Konnov, A. A. 2000, in *28th Symp. (Int.) on Combustion*, Edinburgh, Abstr. Symp. Pap., 317
- Le Teuff, Y. H., Millar, T. J., & Markwick, A. J. 2000, *A&AS*, 146, 157
- Leenaarts, J., & Wedemeyer-Böhm, S. 2005, *A&A*, 431, 687
- Ludwig, H.-G. 1992, Ph.D. Thesis, University of Kiel
- Millar, T. J., Bennett, A., Rawlings, J. M. C., Brown, P. D., & Charnley, S. B. 1991, *A&AS*, 87, 585
- Mitchell, G. F. 1984, *ApJS*, 54, 81
- Noyes, R. W., & Hall, D. N. B. 1972a, *BAAS*, 4, 389
- Noyes, R. W., & Hall, D. N. B. 1972b, *ApJ*, 176, L89
- Palla, F., Salpeter, E. E., & Stahler, S. W. 1983, *ApJ*, 271, 632
- Petuchowski, S. J., Dwek, E., Allen, J. E., & Nuth, J. A. 1989, *ApJ*, 342, 406
- Prasad, S. S., & Huntress, W. T. 1980, *ApJS*, 43, 1
- Skartlien, R. 1998, Ph.D. Thesis, University of Oslo, Norway
- Solanki, S. K., Livingston, W., & Ayres, T. 1994, *Science*, 263, 64
- Stein, R. F., & Nordlund, A. 1989, *ApJ*, 342, L95
- Uitenbroek, H. 2000, *ApJ*, 531, 571
- Uitenbroek, H. 2001, *ApJ*, 557, 389
- Uitenbroek, H., Noyes, R. W., & Rabin, D. 1994, *ApJ*, 432, L67
- Vernazza, J. E., Avrett, E. H., & Loeser, R. 1981, *ApJS*, 45, 635
- Wedemeyer, S. 2003, Ph.D. Thesis, University of Kiel, http://e-diss.uni-kiel.de/diss_764/
- Wedemeyer, S., Freytag, B., Steffen, M., Ludwig, H.-G., & Holweger, H. 2004, *A&A*, 414, 1121 (W04)
- Westley, F. 1980, *NSRDS-NBS*, 67, 1 (W80)
- Wiedemann, G., Ayres, T. R., Jennings, D. E., & Saar, S. H. 1994, *ApJ*, 423, 806